Journal of Energy Chemistry 73 (2022) 599–606

Contents lists available at ScienceDirect

Journal of Energy Chemistry

journal homepage: www.elsevier.com/locate/jechem

http://www.journals.elsevier.com/journal-of-energy-chemistry/

Research article

In-depth understanding of ionic liquid assisted perovskite film formation mechanism for two-step perovskite photovoltaics

Fei Wang [a,c,1], Patrick Wai-Keung Fong [b,1], Zhiwei Ren [b,e,*], Hai-Lun Xia [a], Kang Zhou [a], Kai Wang [f], Jiajie Zhu [g], Xiaoxi Huang [a], Xiao-Yuan Liu [a], Hao Wang [a], Yumeng Shi [d], Haoran Lin [a], Quanyao Zhu [c,*], Gang Li [b,e,*], Hanlin Hu [a,*]

[a] Hoffman Institute of Advanced Materials, Shenzhen Polytechnic, Shenzhen 518055, Guangdong, China
[b] Department of Electronic and Information Engineering, Research Institute for Smart Energy (RISE), The Hong Kong Polytechnic University, Hong Kong 999077, China
[c] State Key Laboratory of Advanced Technology for Materials Synthesis and Processing, School of Materials Science and Engineering, Wuhan University of Technology, Wuhan 43007, Hubei, China
[d] International Collaborative Laboratory of 2D Materials for Optoelectronics Science and Technology of Ministry of Education, Institute of Microscale Optoelectronics, Shenzhen University, Shenzhen 518060, Guangdong, China
[e] The Hong Kong Polytechnic University Shenzhen Research Institute, Shenzhen 518057, Guangdong, China
[f] Institute of Flexible Electronics, Northwestern Polytechnical University, Xi'an 710072, Shannxi, China
[g] School of Physics Science and Engineering, Tongji University, Shanghai 200092, China

ARTICLE INFO

Article history:
Received 5 May 2022
Revised 11 June 2022
Accepted 19 June 2022
Available online 25 June 2022

Keywords:
Halide vacancies
Perovskite solar cells
Two-step method
Ionic liquid

ABSTRACT

Ionic liquids (ILs) have been widely applied in the one-step fabrication of perovskite with noticeable enhancement in the device performance. However, in-depth mechanism of ionic-liquid-assisted perovskite film formation is not well understood for also important two-step perovskite fabrication method, with better control of crystallization behavior. In this work, we introduced ionic liquid methylammonium formate (MAFa) into organic salt to produce perovskite film via a two-step method. Systematic investigations on the influence of MAFa on the perovskite thin film formation mechanism were performed. Ionic liquid is shown to assist lowering the perovskite formation enthalpy upon the density functional theory (DFT) calculation, leading to an accelerated crystallization process evidenced by *in-situ* UV-Vis absorption measurement. A gradient up-down distribution of ionic liquid has been confirmed by time-of-flight SIMS. Importantly, besides the surface passivation, we found the $HCOO^-$ can diffuse into the perovskite crystals to fill up the halide vacancies, resulting in significant reduction of trap states. Uniform perovskite films with significantly larger grains and less defect density were prepared with the help of MAFa IL, and the corresponding device efficiency over 23% was obtained by two-step process with remarkably improved stability. This research work provides an efficient strategy to tune the morphology and opto-electronic properties of perovskite materials *via* ionic-liquid-assisted two-step fabrication method, which is beneficial for upscaling and application of perovskite photovoltaics.

1. Introduction

As a promising printable solar technology [1], Hybrid organic–inorganic perovskite solar cells (PSCs) have attracted extensive research interests because of their ascendant power conversion efficiencies (PCEs), excellent light absorption performance, low manufacturing cost, facile production process, and tunable band-gap [2–6]. In the past decade, the PCEs of perovskite solar cells gradually increased from the debut of 3.8% to 25.7%, comparable to commercial silicon solar cells [7–13]. PSCs with the long-term operational stability [14], manufacturability [15] and outstanding PCEs show great application potential for deployment as the next generation of photovoltaic devices. Among all the different factors, compositional engineering has always been regarded as an important factor in affecting the stability and efficiency of PSCs. Enormous effort has been made to investigate the influence of the composition of perovskite on the performance of PSCs. In contrast to the pure cation at the early development of perovskite, double or multiple cation compositions have been widely applied in the

* Corresponding authors.
E-mail addresses: zhiweipv.ren@polyu.edu.hk (Z. Ren), cglamri@whut.edu.cn (Q. Zhu), gang.w.li@polyu.edu.hk (G. Li), hanlinhu@szpt.edu.cn (H. Hu).
[1] These authors contributed equally to this work.

https://doi.org/10.1016/j.jechem.2022.06.040

perovskite materials to demonstrate improved device performance both in the stability and efficiency [7]. Despite this, the defects both in the bulk and at the surface of perovskite layer are the detrimental factors that limit the further improvement of long-term stability and photoelectric performance of PSCs [16,17].

To overcome the abovementioned limiting factors, different types of additives have been used in the perovskite precursor solution to control the crystal growth of perovskite and improve the film morphology, so as to effectively suppress the defect density [18–21]. Among all of them, ionic liquids (ILs) are the considered environmentally friendly and green additives due to their non-volatile characteristics [22,23]. In addition, ILs offer benefits like materials availability, high carrier mobility, solvate capability, as well as thermal and electrochemical stability, which have been widely applied in perovskite solar cells [24–27], especially for one-step fabrication method. Akin et al. employed 1-hexyl-3-methylimidazolium iodide (HMII) IL as an additive in one-step $FAPbI_3$-based PSCs to regulate the film morphology [28]. Wei and colleagues incorporated 1-ethyl-3-methylimidazolium trifluoroacetate (EMIMTFA) IL into PSCs through one-step fabrication method to passivate the interfacial defects between the perovskite layer and the electron transfer layer [29]. Bai et al. incorporated IL 1-butyl-3-methylimidazolium tetrafluoroborate ($BMIMBF_4$) into the perovskite film in one-step fabrication method to increase the photovoltaic device efficiency and stability through the manipulation of the crystallization and morphology, and revealed the indepent effect of both $[BMIM]^+$ and $[BF_4]^-$ on the performance of PSCs [30]. Moreover, ionic liquids with other anions such as bromine (Br^-), chloride (Cl^-), and iodine (I^-) have also been widely studied for one-step fabrication of PSCs [28,31]. Recently, another pseudo-halide anion, formate ($HCOO^-$) in ionic liquids, has also been demonstrated to control the grain size distribution in perovskite film prepared by one-step method [32]. However, these ILs studies dominantly focused on one-step perovskite films and resultant devices. Compared to the one-step method, two-step perovskite fabrication method is highly preferred by industry for scaling-up process due to the higher reproducibility and better control of perovskite material crystallization process [33]. Up to date, only few studies have been carried out on the IL-assisted two-step perovskite method and the in-depth mechanism of IL-assisted perovskite film evolution is still poorly understood.

Here, we incorporate IL methylammonium formate (MAFa) into organic salt to fabricate perovskite solar cells by two-step method, and systematically investigate the function of $HCOO^-$ on the crystallization kinetics, defect states, thin film morphology, and the resultant device performance. MAFa is shown to accelerate the perovskite crystallization process evidenced by *in-situ* UV-Vis absorption measurement, which is attributed to the lowered IL-assisted perovskite formation enthalpy, supported by the DFT calculation. With the help of time-of-flight secondary-ion mass spectrometry (TOF-SIMS), the distribution of IL has been confirmed in the vertical direction with respect to the substrate surface. Most importantly, we discovered that the size of $HCOO^-$ is small enough to effectively reduce the defect density by filling up the halide vacancies within the perovskite bulk materials. This can significantly suppress the charge-carrier recombination and prolong the photoluminescence lifetime, resulting in remarkably improved device performance. With the assistance of IL, we successfully demonstrated a highly stable and efficient PSC with PCE exceeding 23% via two-step sequential deposition method. The detailed understanding of IL assisted perovskite thin film evolution mechanism revealed in this work, including the crystallization kinetics and suppression of trap density of high-quality perovskite film formation via two-step deposition, which is beneficial for the upscaling and deployment of PSCs in the near future.

2. Experimental section

Materials: ITO glass substrates with a sheet resistance of ca. 9 Ω sq^{-1} were purchased from OPVTECH Inc. Formamidinium Iodide (FAI), methylammonium chloride (MACl), methylammonium bromide (MABr), and ionic liquids MAFa were supplied from Xi'an Polymer Light Technology Crop. PbI_2 (99.8%), bis (trifluoromethane) sulfonimide lithium salt (Li-TFSI, 99%), 4-tert-butylpyridine (tBP, 96%) and CsI (99.99%) were supplied from Sigma-Aldrich. Tin (IV) oxide (SnO_2) Quantum Dots (QDs) precursor was prepared according to the previously reported references [34]. DMF, DMSO, IPA and acetonitrile were purchased from TCI. Spiro-OMeTAD (purity. 99.5%) was purchased from Feiming Science and Technology Co., Ltd. All chemicals were used as received without further treatment.

Devices fabrications: ITO substrates were sequentially rinsed by sonication in detergent, deionized (DI) water, acetone, and isopropanol for 30 min, respectively, and then dried under nitrogen gas. Cleaned ITO substrates were treated with ultraviolet-ozone for 30 min, followed by deposition of a SnO_2 electron transporting layer on the substrate by spin-coating the SnO_2 QDs precursor (1.3 M) at 4000 r min^{-1} for 30 s, and subsequently annealed at 150 °C for 30 min on a hotplate. The perovskite layer was fabricated in the glovebox through a modified two-step sequential method according to the literature. First, 1.3 M PbI_2 precursor was dissolved in 950 mL DMF and 50 μL CsI solution (1.5 M, 390 mg CsI was dissolved in 1 mL DMSO). The above solution was then spin-coated on the SnO_2/ITO substrate at 1500 r min^{-1} for 30 s, and dried at 70 °C for 1 min. Thereafter, a mixture solution of FAI:MABr:MACl (60 mg: 6 mg: 6 mg in 1 mL IPA and x μL MAFa, x represents the volume of the ionic liquid, x = 0, 2 and 5) was dropped on the PbI_2 film at 1500 r min^{-1} for 30 s. The as-cast perovskite film was annealed at 105 °C for 30 min. The spiro-OMeTAD solution was composed of 72.3 mg spiro-OMeTAD, 30 μL TBP, and 35 μL Li-TFSI solution (260 mg in 1 mL acetonitrile) in 1 mL chlorobenzene, and then spin-coated on perovskite film at 4000 r min^{-1} for 30 s. Finally, a 100 nm Au electrode was deposited by thermal evaporation.

Characterization: The time-resolved *in-situ* absorption measurements were performed using an F20-UVX spectrometer equipped with tungsten halogen and deuterium light sources (Filmetrics, Inc.). Most of the measurements were performed with an integration time of 0.2 s (thin perovskite layer) and 1 s (thick perovskite layer) per transmission spectrum. The UV-vis absorbance is calculated from the transmission spectrum, using the equation: $A(\lambda) = -\log_{10}(T)$, where $A(\lambda)$ is the absorbance at a certain wavelength (λ) and T is the calibrated transmitted radiation.

The *J-V* characteristics of the PSCs devices were measured by IVS-KA6000 Enlitech sunlight simulator equipped with an AM 1.5 filter at 100 mW cm^{-2} and Keithley SMU source after correcting the light intensity with a standard calibration cell. The corresponding EQE spectrum was acquired in air by a QE-R system from Enli Technology Co. Ltd. Static PL and TRPL measurements of perovskite film were recorded by Edinburgh FLSP1000 spectrophotometer equipped with an excitation source of 440 nm picosecond pulsed diode laser.

SEM studies were conducted on a Zeiss Sigma300 to observe the morphology of perovskite thin film. AFM characterizations were conducted on a Bruker Dimension ICON. X-ray diffractometer spectrum of perovskite film with scanning angle from 3° to 40° (2θ) was recorded by Bruker D8 Advance.

TOF-SIMS experiments were performed using a TOF-SIMS V spectrometer (IONTOF GmbH, Münster, Germany). A pulsed 30 keV Bi^+ ion beam was used as the primary ion beam for all measurements, with a target current of 1 pA. The analysis area was

100 mm × 100 mm. For depth profiling, a 2 keV Cs ion source was chosen to sputter the sample surface during analysis, with a sputter area of 300 mm × 300 mm. The measurement was conducted in the non-interlaced mode. Besides, an electron flood gun was used to compensate for surface charging during all measurements. All data were obtained and analyzed using the IONTOF instrument software.

Computational method: All the calculations are conducted in the framework of the density functional theory with the projector augmented plane-wave method, which was carried out in the Vienna ab initio simulation package. The generalized gradient approximation proposed by Perdew, Burke, and Ernzerhof is selected for the exchange-correlation potential. The long range van der Waals interaction is taken into account by DFT-D3 approach. The cut-off energy for plane wave is set to 400 eV. The energy criterion is set to 10^{-5} eV in iterative solution of the Kohn-Sham equation. Supercells containing 3 × 3 × 1 unit cells (324 atoms) are built to model the defective structures. The Brillouin zone integration is performed at the Gamma point. All the structures are relaxed until the residual forces on the atoms have declined to less than 0.05 eV $Å^{-1}$.

3. Results and discussion

A PbI_2 layer doped with Cs^+ was deposited on the ITO/SnO_2 substrate. Then organic salts—FAI mixed with MABr and MACl—were coated on top of the PbI_2 layer, followed by thermal annealing to convert into pristine perovskite film (Fig. S1). The doping of Cs^+ ions enhances the light absorption and facilitates the formation of larger grains for the perovskite film [7,35,36]. The introduction of a small amount of MABr and MACl further improves the phase stability of perovskite and assists in the growth of perovskite crystals, respectively [37]. For IL-assisted perovskite photoactive layer, IL MAFa was specially designed to mix with same organic salt mixture to form IL-assisted perovskite film (Fig. S1). The scanning electron microscopy (SEM) was first utilized to examine the morphology for both the pristine and IL-assisted perovskite films. Compared to the pristine one (Fig. 1a), a 0.2% MAFa IL-assisted perovskite film exhibits a more uniform morphology with a noticeable increased grain size (Fig. 1b). The average grain size is 319.1 nm for the pristine, while it remarkably increases to 798.0 nm for the MAFa-assisted one as indicated by the insets of Fig. 1(a and b), respectively. It is worth mentioning that relatively small grain-size perovskite cannot be observed in the IL-assisted perovskite thin film since the existence of IL can significantly inhibit the formation of small perovskite grains. In our work, liquid microdomains contributed by the nonvolatile IL (MAFa) in the perovskite or its intermediate film can directly facilitate the grain growth via intensified Ostwald ripening [38] and coarsening process [39], leading to increased grain size via prohibiting the small grain growth as we discussed above. These results are very consistent with the phenomenon that has been reported in [32,40]. The increased grain size for the IL-assisted perovskite film is also confirmed by atomic force microscopy (AFM), as shown in Fig. S2. Furthermore, the surface roughness of the IL-assisted perovskite film decreased which is attributed to the increased grain size [40].

To study the effect of IL on the perovskite crystallization kinetics, *in-situ* UV-Vis absorption measurements were performed systematically on both the pristine and IL-assisted samples at the thermal annealing stage. The conversion processes of pristine and IL-assisted samples during thermal annealing treatment were tracked by time-resolved *in-situ* absorption spectroscopy in Fig. 1 (c and d), respectively. The results clearly show that the absorption of the perovskite precursor film red-shifts at the early stage of the thermal annealing process, indicative of the gradual solidification, and conversion processes of perovskite material. Finally, the absorption spectrum stabilizes, attributed to the complete conversion of perovskite. In contrast to the pristine one, we observed prominent differences for the 0.2% MAFa IL-assisted one: the absorption spectrum takes shorter time to stabilize comparing to that of the pristine one. This difference reveals an accelerated perovskite conversion process by the addition of a small amount of IL into the organic salt. To clearly illustrate this observation, extracted absorption intensities at 600 nm (as indicated by the white dash lines in Fig. 1c and d) as a function of time were plotted as shown on top of the corresponding *in-situ* absorption spectrum. The solidification of perovskite for the control sample and 0.2% MAFa IL-assisted sample are 40 and 20 s, respectively. Similar phenomenon has been observed for the 0.5% MAFa IL-assisted sample, exhibiting shorter conversion time, as shown in Fig. S3. These results suggest that the addition of ionic liquids facilitates the formation of perovskite, resulting in an accelerated perovskite crystallization kinetics. To better elucidate this phenomenon, DFT calculation has been applied to simulate the formation process of perovskite with the halide vacancies occupied by $HCOO^-$ as shown in the chemical Eq. (1). From the DFT calculation results, the formation energy (enthalpy), as shown in chemical Eq. (2), and the binding energies for the $HCOO^-$ substitution at the I vacancy site were calculated to − 2.87 and − 5.04 eV, respectively, which show that this is a spontaneous process. The DFT results agree well with the above *in-situ* UV-Vis absorption results, which is also confirmed by the faster conversion process for the IL-assisted perovskite as recorded by the optical camera in supporting information Fig. S4.

$$FAHCOO + FAPbI_3(V_I + V_{FA}) \rightarrow FAPbI_3(HCOO_I) \quad (1)$$

$$H = E[FAPbI_3(HCOO_I)]\text{-}E[FAHCOO]\text{-}E[FAPbI_3(VI + V_{Ma})] \quad (2)$$

TOF-SIMS signals with both negative and positive secondary ions were performed to analyze ions depth distribution of IL MAFa to probe perovskite structure with 0.2% MAFa. As expected, $(CH_3NH_3^+)_m(HCOO^-)_n$ is not detected in the control sample (Fig. 2a) whereas it exists in the 0.2% MAFa-perovskite sample (Fig. 2b). Based on the ions profiling results from TOF-SIMS, the corresponding 3D distributions of anion ions are drawn in Fig. 2(c and d) and Fig. S5 to illustrate that MAFa IL mainly distributes near the surface, decreases exponentially and reaches stable minimal value ($\sim 2 \times 10^0$) at a depth about half of the perovskite thickness. Similar results can be obtained in the positive ion mode as shown in Fig. S6. Movever, the existence of $(CH_3NH_3^+)_m(HCOO^-)_n$ in perovskite film with 0.2% MAFa is observed in the mass spectra in Fig. 2(e and f) and Fig. S7. These results prove that IL MAFa mainly exists near the surface and grain boundaries of perovskite films, which effectively passivate the corresponding defects, resulting in the formation of high quality thin film.

For further investigation of the impact of the IL MAFa on the perovskite film, X-ray diffraction (XRD) measurements were conducted for perovskite films without and with 0.2% MAFa. The XRD spectra in Fig. 3(a) show identical peak positions at around 14.02° for both control and 0.2% MAFa-perovskite film, which indicates that the IL MAFa does not lead to polymorphism or variation of lattice. Similar result has also been reported in perovskite thin film prepared by one-step method when small amount of IL MAFa is added into the precursor solution [32]. UV-vis absorption and photoluminescence measurements were measured to show almost identical absorption threshold and photoluminescence peak position for both the control and 0.2% MAFa-perovskite films, demonstrating the retention of lattice which is consistent to the XRD findings (Fig. 3b and c). Interestingly, the PL intensity and photoluminescence lifetime of the 0.2% MAFa-perovskite film are stronger and longer than that of the control sample, which is attributed to a

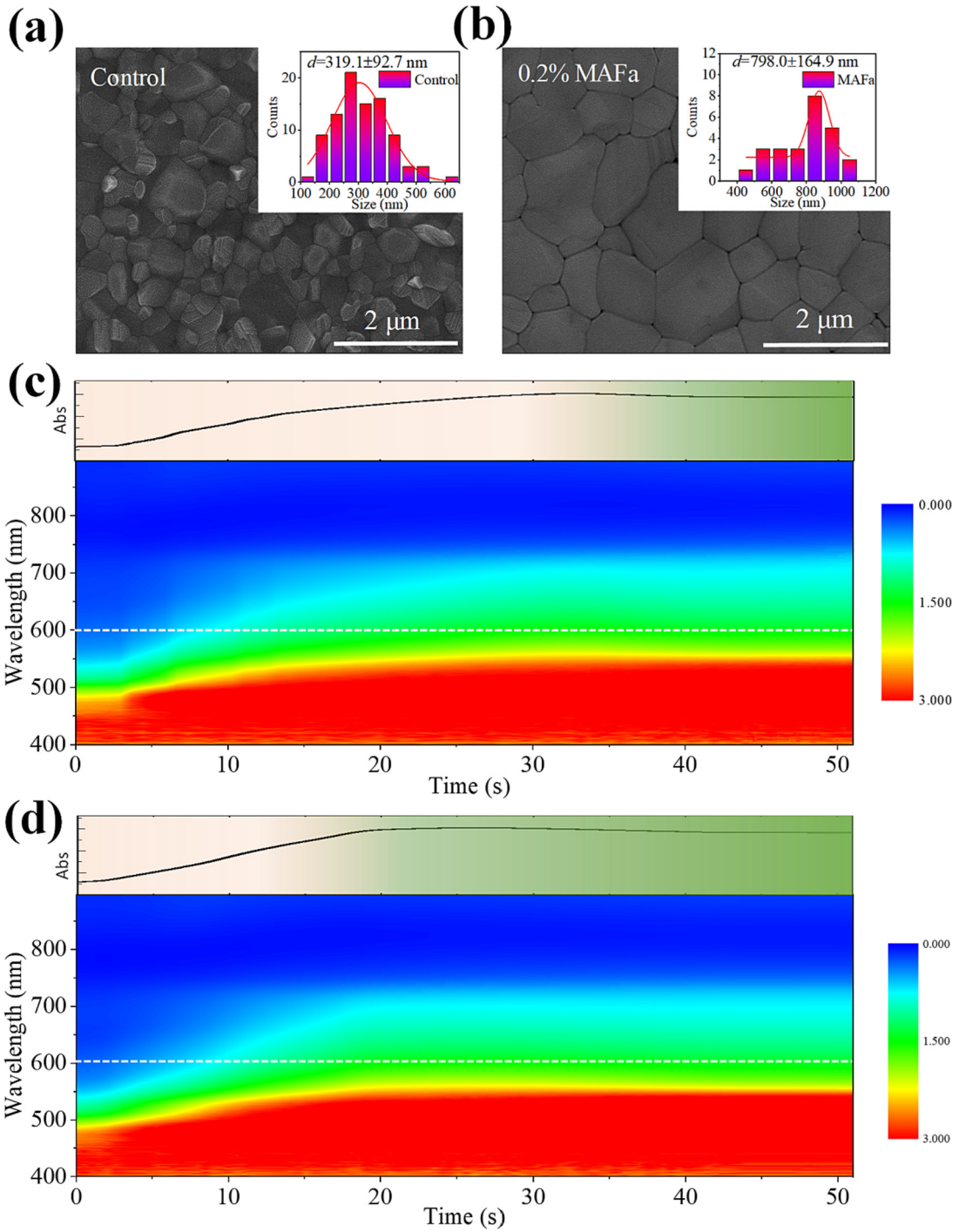

Fig. 1. SEM images of (a) control and (b) 0.2% MAFa-perovskite film. The insets show the grain size distribution of the corresponding perovskite films. Time-resolved *in situ* UV-vis absorption spectra of (c) control and (d) 0.2% MAFa-perovskite film in annealing process.

remarkably reduction in defect density and non-radiative recombination centers (Fig. 3c and d, Fig. S8). It is interesting to note that perovskite film prepared by a higher MAFa concentration of 0.5% exhibits a faster PL decay than that of the pristine one (Fig. S3). It is believed that excessive addition of ionic liquid results in an increase in defects by generating irregular grains within the perovskite bulk material [41]. To further verify the effect of ionic liquid in perovskite film on the reduction of non-radiation recombination centers, EQE_{EL} of the PSCs fabricated without and with 0.2% MAFa IL were measured (Fig. 3e and f). The EQE_{EL} values of the control and the 0.2% MAFa-device are 1.16% and 3.63% under an injection current of 23.69 mA cm^{-2} and 24.23 cm^{-2}, respectively. These results effectively show that the trap density is remarkably reduced and the non-radiative recombination is significantly suppressed beneficial to the addition of ionic liquids as additives in the perovskite film formation process.

As a classical ionic crystal, perovskite materials always show vacancy states, especially the halide vacancies, within its crystal structure [42]. To shed further light on the impact of IL on the halide vacancies in perovskite materials, density functional theory (DFT) calculations (see the Experimental Section for computational details) were performed on the pristine and IL-modifed perovskite

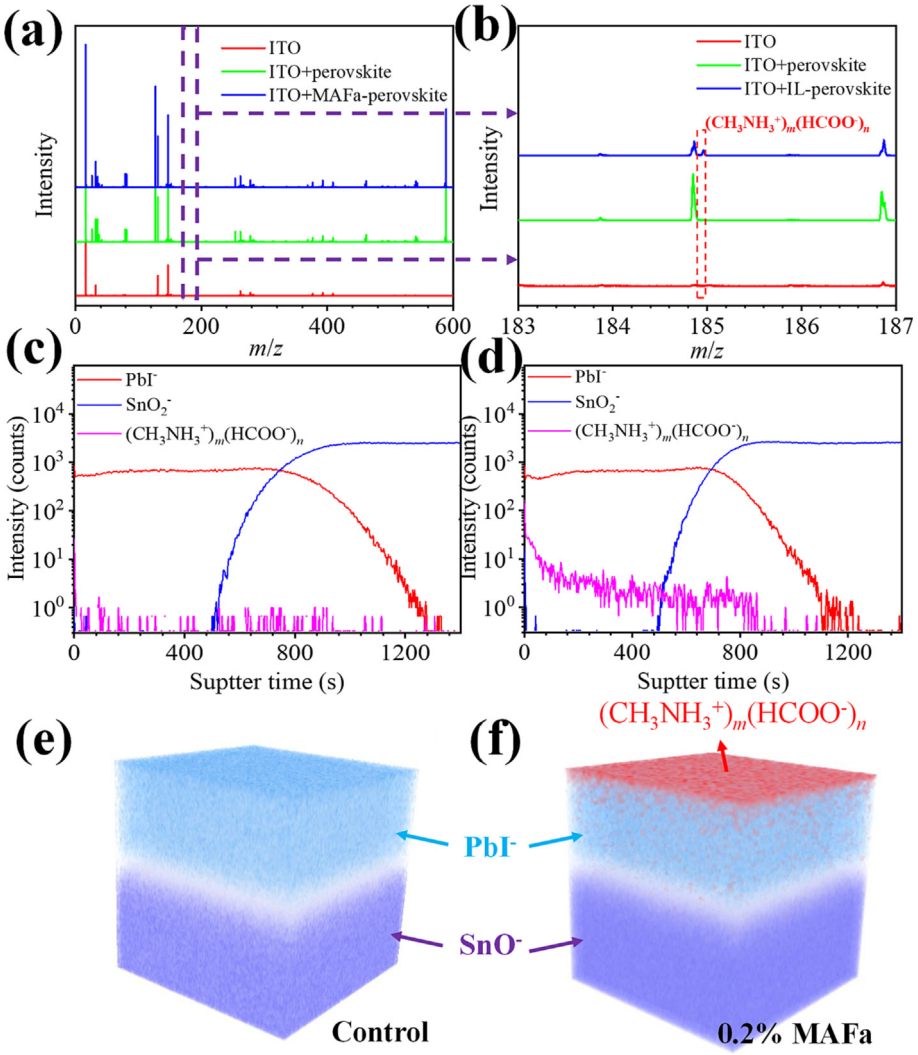

Fig. 2. TOF-SIMS depth profile of PbI^-, SnO_2^- and $(CH_3NH_3^+)_m(HCOO^-)_n$ in (a) control and (b) 0.2% MAFa-perovskite film. 3D distribution of PbI^-, SnO_2^- and $(CH_3NH_3^+)_m(HCOO^-)_n$ in (c) control and (d) 0.2% MAFa-perovskite film from TOF-SIMS measurements. (e, f) Mass spectrum of ITO, perovskite film on ITO and MAFa-perovskite film on ITO in negative ion mode.

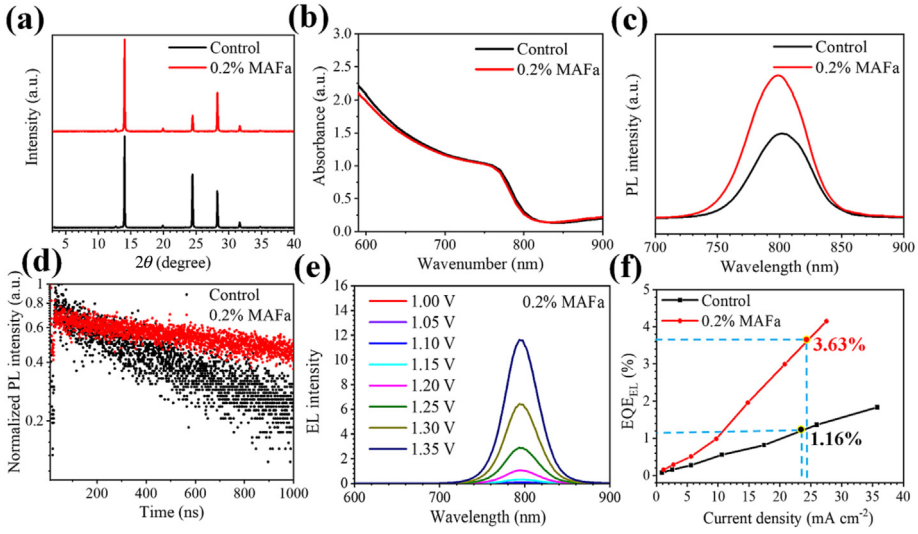

Fig. 3. (a) X-ray diffraction diagram of perovskite films grown without and with 0.2% MAFa. (b) UV-Vis absorption spectra of the perovskite films. (c) Photoluminescence and (d) time-resolved photoluminescence spectra of the perovskite films. (e) EL spectra of the 0.2% MAFa-PSCs under different forward biasing voltages. (f) EQE_{EL} of the control and 0.2% MAFa-PSCs.

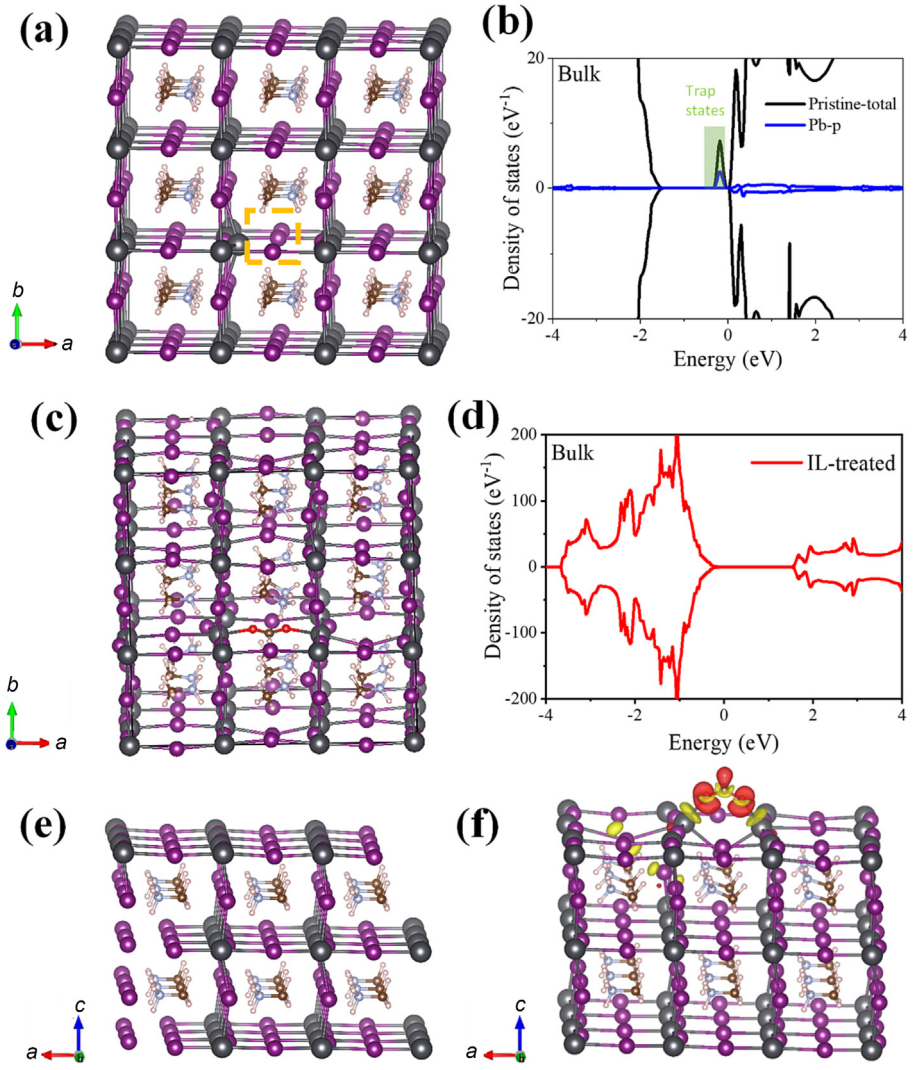

Fig. 4. (a) Crystal structure of perovskite with an iodine vacancy marked by a yellow square and (b) the corresponding density of states function. (c) Crystal structure of perovskite with $HCOO^-$ at the iodine vacancy site and (d) the corresponding density of states function. (e) Crystal structure of perovskite at the surface. (f) Charge density difference between $HCOO^-$ and perovskite surface modified by $HCOO^-$. Red and yellow color indicate charge accumulation and depletion, respectively. Ios values of isosurfaces were set to 0.002 e $borh^{-3}$.

materials as shown in Fig. 4 and Figs. S9 and S10. The structure of the perovskite with an iodine vacancy is illustrated in Fig. 4(a). The trap states induced by iodide vacancy defects typically localized in the nearby Pb atoms and located close to the bottom of the conduction band [43] (Fig. 4b). In the case of the IL-modified structure (Fig. 4c), the $HCOO^-$ turns out to occupy the vacancy site, leading to a suppression of defect states, which recovers the ideal electronic structure of perfect perovskite material (Fig. 4d). The DFT results indicate that the IL assists the growth of high-quality perovskite material through the suppression of halide vacancy states. Fig. 4(e and f) and Fig. S10 show pure and $HCOO^-$-modified surfaces of the perovskite. Charge transfer mainly takes place from the Pb atom to the O atom, showing strong interaction, and $HCOO^-$ species saturate the dangling bonds on the surface of the perovskite.

The space-charge-limited current (SCLC) measurements were also measured to evaluate the effect of 0.2% MAFa on the defect densities of different perovskite films in devcies of the structure ITO/Poly(3,4-ethylenedioxythiophene)/poly(styrenesulfonate) (PEDOT:PSS)/perovskite/2,2′,7,7′-Tetrakis[*N*,*N*-di(4-methoxyphenyl)amino]-9,9′-spirobifluorene (Spiro-OMeTAD)/Au. The defect density (N_t) is calculated by the equation of

$$N_t = \frac{2\varepsilon_r \varepsilon_0 V_{TFL}}{qL^2} \quad (3)$$

where ε_r is the relative dielectric constant and the value taken here is 62.23 [44], ε_0 is the vacuum permittivity, V_{TFL} is the onset voltage of the trap-filled limit region, q is the charge of an electron, and L is the thickness of the perovskite film. V_{TFL} (and the corresponding defect density) values of the control and 0.2% MAFa-perovskite film are 0.55 V (8.89×10^{15} cm^{-3}) and 0.27 V (4.36×10^{15} cm^{-3}), respectively, as shown in Fig. 5(a–c). These results clearly show that the perovskite fabricated by adding 0.2% MAFa IL exhibits a noticeably reduced defect density and is in a good agreement with the DFT calculation that $HCOO^-$ can effectively occupy the halide vacancies for the perovskite crysal both in the bulk and at the surface.

To further examine the influence of the addition of IL MAFa on the device performance, the pristine and 0.2% MAFa-perovskite film were applied to fabricate sandwich-like PSCs with a typical architecture of ITO/SnO_2/perovskite/Spiro-OMeTAD/Au as shown in Fig. 5(d) As shown in the cross-sectional SEM image of MAFa assisted PSC device, a uniform perovskite top layer with a thickness of around 700 nm was equipped in the device. The *J-V* curves of the

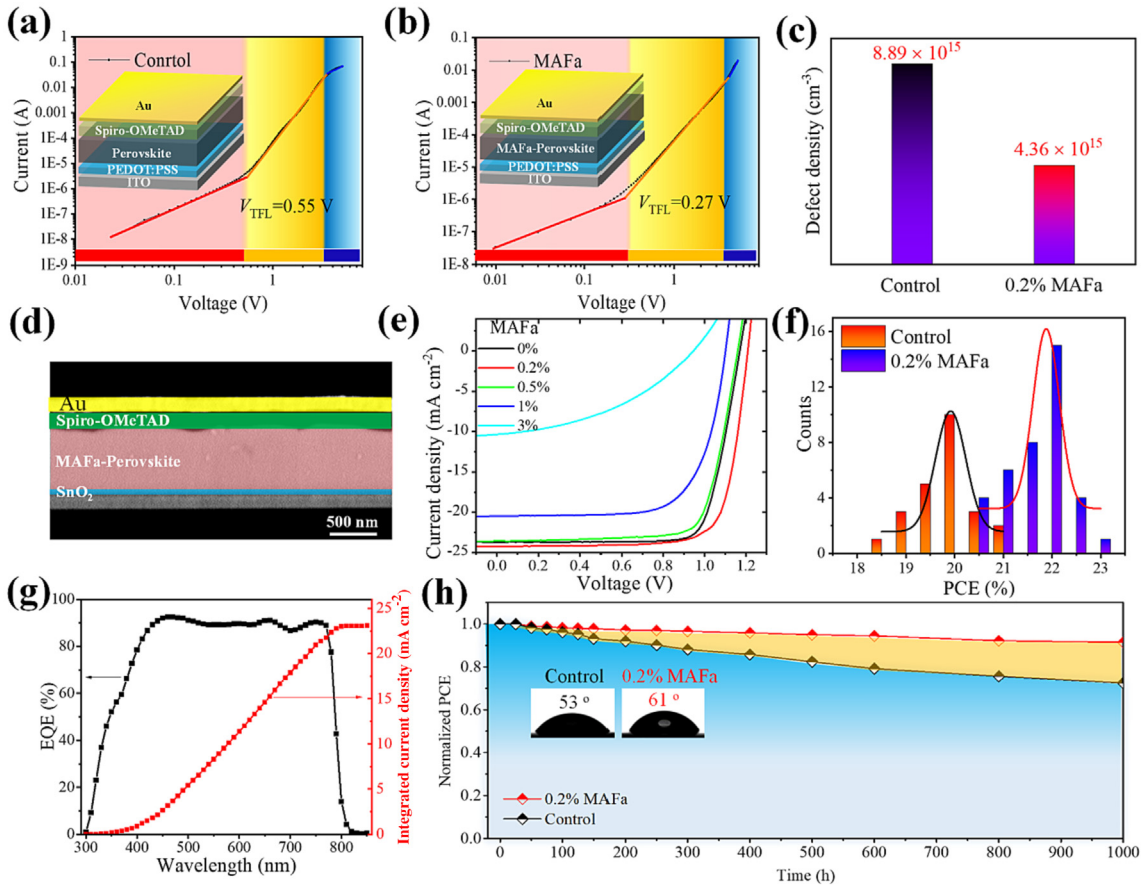

Fig. 5. Characterization of the photovoltaic performance of the PSCs. (a, b) *J-V* characteristics of the control and 0.2% MAFa-perovskite film derived from the SCLC measurements with a structure of ITO/PEDOT:PSS/perovskite/Spiro-OMeTAD/Au. V_{TFL} is expressed as trap-filled limited voltage. (c) Statistics of defect density calculated by SCLC measurements. (d) Cross-sectional SEM image of the perovskite device structure. (e) *J-V* curves of the PSCs with different concentrations of IL MAFa. (f) The distribution of PCEs of the control and 0.2% MAFa-PSCs. (g) EQE and the integrated J_{SC} of the 0.2% MAFa-PSCs. (h) Normalized PCE evolution of the unencapsulated devices measured over 1000 h at 30 °C in ambient dry air (relative humidity ~15%±5%). The insets show the water contact angle of the control and 0.2% MAFa-perovskite film.

PSCs with different amounts of IL MAFa were measured (Fig. 5e). The results show a systematic trend that addition of 0.2% MAFa can improve the photovoltaic performance but excessive amount of MAFa results in the deterioration in the device performance. Statisticial analysis of the PSCs performance with different amounts of MAFa are summarized in Table S1. The PSCs without IL MAFa deliver an average efficiency of 21.26% with an open-circuit voltage (V_{OC}) of 1.17 V, a short circuit current (J_{SC}) of 23.69 mA cm^{-2}, and a fill factor (FF) of 0.767. In contrast, the devices with 0.2% MAFa gain an obvious V_{OC} and FF enhancement, attributed to the lower defect density assisted by the passivation of perovskite halide vacancy defects by $HCOO^-$ and the suppression of non-radiative recombination process. The champion device with 0.2% MAFa has a PCE of 23.11% accompanied by a high V_{OC} of 1.21 V, J_{SC} of 24.23 mA cm^{-2}, and a FF of 0.788. The J_{SC} values obtained from *J-V* curves match well with that derived from the EQE results (23.08 mA cm^{-2}), integrated over the solar spectrum (Fig. 5g). Statistical distribution (from over at least 24 devices in each condition) of the PCE for the pristine and the 0.2% MAFa-PSCs are shown in Fig. 5(f). Not only the average PCE is significantly improved but also the scattering of the PCE distribution is narrowed for the devices prepared by 0.2% MAFa IL. Despite the remarkable improvement in PCE, stability of PSC is another key issue to address. ILs have been regarded as potential alternatives to traditional additives for fabricating stable PSCs [45,46]. As discussed above, the reduction in defect density, especially the halide vacancies, helps to suppress the ion migration and subsequently improve the device stability [47,48]. We found that MAFa modified pervoskite surface provided a better moisture barrier for the bulk perovskite material. The water contact angles of the pristine and MAFa-modified perovskite surface are 53° and 61°, respectively, as shown in the insets in Fig. 5(h). The stability of the unencapsulated control and 0.2% MAFa-perovskite PSCs are evaluated by the PCE as a function of time (Fig. 5h). The unencapsulated 0.2% MAFa-perovskite device demonstrates a better long-term stability and maintains 90% of its original PCE in ambient dry air conditions after 1000 h. Thus, our results show that the addition of MAFa IL with optimal concentration of 0.2% can significantly improve the performance of PSCs both the PCE and long-term stability, attributed to the efficient passivation of halide vacancies.

4. Conclusions

In summary, we have explored the in-depth mechanism of MAFa IL-assisted perovksite film formation process via two-step deposition method, resulting in perovskite photovoltaics with improved device performance. The addition of IL accelerates the perovskite crystallization kinetics with a faster conversion process, evidenced by the *in-situ* UV-Vis absorption spectroscopy. First-principle DFT calculation shows that addition of 0.2% MAFa IL can effectively lower the perovskite formation enthalpy. TOF-SIMS technique probes the distribution of IL within the perovskite layer in normal direction, showing a gradient vertical distribution.

Besides the widely reported surface passivation, we proved that the $HCOO^-$ can diffuse into the perovskite crystals, fill up the halide vacancies and effectively reduce the trap density, which has been confirmed by DFT calculation. Experimentally, the results from SCLC measurement also proved that the trap density has decreased for IL-assisted perovskite film, leading to improved optoelectronic properties. High-quality perovskite films with noticeable large grain were fabricated with the help of ionic liquid via sequential deposition approach. Upon these, we have demonstrated the fabrication of MAFa IL-assisted PSCs of PCE over 23% accompanied by improved stability, attributed to the enhanced moisture barrier and defects suppression. This work provides an effective strategy to manipulate the morphology and optoelectronic properties of perovskite materials, which is beneficial for upscaling manufacture of perovskite photovoltaics.

Declaration of competing interest

The authors declare that they have no known competing financial interests or personal relationships that could have appeared to influence the work reported in this paper.

Acknowledgments

This work was supported by the National Natural Science Foundation of China (Grant Nos. 62004129, 51472189, 22005202), the Shenzhen Science and Technology Innovation Commission (JCYJ20200109105003940), the Research Grants Council of Hong Kong (GRF grant 15221320, CRF C5037-18G, C7018-20G), and the Hong Kong Polytechnic University Funds (Sir Sze-yuen Chung Endowed Professorship Fund (8-8480), and RISE (Q-CDA5)).

Appendix A. Supplementary data

Supplementary data to this article can be found online at https://doi.org/10.1016/j.jechem.2022.06.040.

References

[1] S.H. Bae, H. Zhao, Y.T. Hsieh, L. Zuo, N. De Marco, Y.S. Rim, G. Li, Y. Yang, Chem 1 (2016) 197–219.
[2] Y. Ma, Q. Zhao, J. Energy Chem. 64 (2021) 538–560.
[3] M.A. Green, A. Ho-Baillie, H.J. Snaith, Nat. Photonics 8 (2014) 506–514.
[4] J.P. Correa-Baena, M. Saliba, T. Buonassisi, M. Grätzel, A. Abate, W. Tress, A. Hagfeldt, Science 358 (2017) 739–744.
[5] H. Hu, M. Qin, P.W.K. Fong, Z. Ren, X. Wan, M. Singh, C.J. Su, U.S. Jeng, L. Li, J. Zhu, M. Yuan, X. Lu, C.W. Chu, G. Li, Adv. Mater. 33 (2021) 2006238.
[6] H. Hu, Z. Ren, P.W.K. Fong, M. Qin, D. Liu, D. Lei, X. Lu, G. Li, Adv. Funct. Mater. 29 (2019) 1900092.
[7] M. Qin, H. Xue, H. Zhang, H. Hu, K. Liu, Y. Li, Z. Qin, J. Ma, H. Zhu, K. Yan, G. Fang, G. Li, U.-S. Jeng, G. Brocks, S. Tao, X. Lu, Adv. Mater. 32 (2020) 2004630.
[8] G. Yang, Z. Ren, K. Liu, M. Qin, W. Deng, H. Zhang, H. Wang, J. Liang, F. Ye, Q. Liang, H. Yin, Y. Chen, Y. Zhuang, S. Li, B. Gao, J. Wang, T. Shi, X. Wang, X. Lu, H. Wu, J. Hou, D. Lei, S.K. So, Y. Yang, G. Fang, G. Li, Nat. Photonics 15 (2021) 681–689.
[9] Y.-W. Jang, S. Lee, K.M. Yeom, K. Jeong, K. Choi, M. Choi, J.H. Noh, Nat. Energy 6 (2021) 63–71.
[10] N. Li, X. Niu, L. Li, H. Wang, Z. Huang, Y. Zhang, Y. Chen, X. Zhang, C. Zhu, H. Zai, Y. Bai, S. Ma, H. Liu, X. Liu, Z. Guo, G. Liu, R. Fan, H. Chen, J. Wang, Y. Lun, X. Wang, J. Hong, H. Xie, D.S. Jakob, X.G. Xu, Q. Chen, H. Zhou, Science 373 (2021) 561–567.
[11] M. Jeong, I.W. Choi, E.M. Go, Y. Cho, M. Kim, B. Lee, S. Jeong, Y. Jo, H.W. Choi, J. Lee, J.H. Bae, S.K. Kwak, D.S. Kim, C. Yang, Science 369 (2020) 1615–1620.
[12] M.J. Jeong, K.M. Yeom, S.J. Kim, E.H. Jung, J.H. Noh, Energy Environ. Sci. 14 (2021) 2419–2428.
[13] X. Li, Z. Shi, F. Behrouznejad, M. Hatamvand, X. Zhang, Y. Wang, F. Liu, H. Wang, K. Liu, H. Dong, F. Mudasar, J. Wang, A. Yu, Y. Zhan, J. Energy Chem. 67 (2022) 1–7.
[14] D.H. Kang, Y.J. Park, Y.S. Jeon, N.G. Park, J. Energy Chem. 67 (2022) 549–554.
[15] K. Liu, P.W.K. Fong, Q. Liang, G. Li, Trends Chem. 3 (2021) 747–764.
[16] Q. Jiang, Y. Zhao, X. Zhang, X. Yang, Y. Chen, Z. Chu, Q. Ye, X. Li, Z. Yin, J. You, Nat. Photonics 13 (2019) 460–466.
[17] W. Cao, Z. Hu, Z. Lin, X. Guo, J. Su, J. Chang, Y. Hao, J. Energy Chem. 68 (2022) 420–438.
[18] Z. Wu, S.R. Raga, E.J. Juarez-Perez, X. Yao, Y. Jiang, L.K. Ono, Z. Ning, H. Tian, Y. Qi, Adv. Mater. 30 (2018) 1703670.
[19] S. Liu, Y. Guan, Y. Sheng, Y. Hu, Y. Rong, A. Mei, H. Han, Adv. Energy Mater. 10 (2020) 1902492.
[20] Y. Niu, D. He, Z. Zhang, J. Zhu, T. Gavin, P. Falaras, L. Hu, J. Energy Chem. 68 (2022) 12–18.
[21] Z. Wang, S. You, G. Zheng, Z. Tang, L. Zhang, J. Zhang, X. Li, X. Gao, J. Energy Chem. 69 (2022) 406–413.
[22] C. Liang, H. Gu, Y. Xia, Z. Wang, X. Liu, J. Xia, S. Zuo, Y. Hu, X. Gao, W. Hui, L. Chao, T. Niu, M. Fang, H. Lu, H. Dong, H. Yu, S. Chen, X. Ran, L. Song, B. Li, J. Zhang, Y. Peng, G. Shao, J. Wang, Y. Chen, G. Xing, W. Huang, Nat. Energy 6 (2021) 38–45.
[23] L. Chao, T. Niu, H. Gu, Y. Yang, Q. Wei, Y. Xia, W. Hui, S. Zuo, Z. Zhu, C. Pei, X. Li, J. Zhang, J. Fang, G. Xing, H. Li, X. Huang, X. Gao, C. Ran, L. Song, L. Fu, Y. Chen, W. Huang, Research 2020 (2020) 2616345.
[24] L. Chao, T. Niu, W. Gao, C. Ran, L. Song, Y. Chen, W. Huang, Adv. Mater. 33 (2021) 2005410.
[25] T. Niu, L. Chao, W. Gao, C. Ran, L. Song, Y. Chen, L. Fu, W. Huang, ACS Energy Lett. 6 (2021) 1453–1479.
[26] Y. Chen, Y. Xu, J. Liu, Y. Lin, J. Hu, C. Cao, Y. Xia, Y. Chen, J. Energy Chem. 71 (2022) 445–451.
[27] D. Gao, L. Yang, X. Ma, X. Shang, C. Wang, M. Li, X. Zhuang, B. Zhang, H. Song, J. Chen, C. Chen, J. Energy Chem. 69 (2022) 659–666.
[28] S. Akin, E. Akman, S. Sonmezoglu, Adv. Funct. Mater. 30 (2020) 2002964.
[29] N. Wei, Y. Chen, X. Wang, Y. Miao, Z. Qin, X. Liu, H. Wei, Y. Zhao, Adv. Funct. Mater. 32 (2021) 2108944.
[30] S. Bai, P. Da, C. Li, Z. Wang, Z. Yuan, F. Fu, M. Kawecki, X. Liu, N. Sakai, J.T.W. Wang, S. Huettner, S. Buecheler, M. Fahlman, F. Gao, H.J. Snaith, Nature 571 (2019) 245–250.
[31] R. Xia, X.-X. Gao, Y. Zhang, N. Drigo, V.I.E. Queloz, F.F. Tirani, R. Scopelliti, Z. Huang, X. Fang, S. Kinge, Z. Fei, C. Roldán-Carmona, M.K. Nazeeruddin, P.J. Dyson, Adv. Mater. 32 (2020) 2003801.
[32] J.Y. Seo, T. Matsui, J. Luo, J.P. Correa-Baena, F. Giordano, M. Saliba, K. Schenk, A. Ummadisingu, K. Domanski, M. Hadadian, A. Hagfeldt, S.M. Zakeeruddin, U. Steiner, M. Grätzel, A. Abate, Adv. Energy Mater. 6 (2016) 1600767.
[33] Q. Jiang, Z. Chu, P. Wang, X. Yang, H. Liu, Y. Wang, Z. Yin, J. Wu, X. Zhang, J. You, Adv. Mater. 29 (2017) 1703852.
[34] Z. Ren, K. Liu, H. Hu, X. Guo, Y. Gao, P.W.K. Fong, Q. Liang, H. Tang, J. Huang, H. Zhang, M. Qin, L. Cui, H.T. Chandran, D. Shen, M.F. Lo, A. Ng, C. Surya, M. Shao, C.S. Lee, X. Lu, F. Laquai, Y. Zhu, G. Li, Light Sci. Appl. 10 (2021) 239.
[35] M. Saliba, T. Matsui, J.Y. Seo, K. Domanski, J.P. Correa-Baena, M.K. Nazeeruddin, S.M. Zakeeruddin, W. Tress, A. Abate, A. Hagfeldt, M. Grätzel, Energy Environ. Sci. 9 (2016) 1989–1997.
[36] C. Zhang, Y. Wang, X. Lin, T. Wu, Q. Han, Y. Zhang, L. Han, J. Mater. Chem. A 9 (2021) 1372–1394.
[37] W.S. Yang, J.H. Noh, N.J. Jeon, Y.C. Kim, S. Ryu, J. Seo, S. Il Seok, Science 348 (2015) 1234–1237.
[38] A. Ummadisingu, L. Steier, J.-Y. Seo, T. Matsui, A. Abate, W. Tress, M. Grätzel, Nature 545 (2017) 208–212.
[39] S. Yang, Y.C. Zheng, Y. Hou, X. Chen, Y. Chen, Y. Wang, H. Zhao, H.G. Yang, Chem. Mater. 26 (2014) 6705–6710.
[40] W. Hui, L. Chao, H. Lu, F. Xia, Q. Wei, Z. Su, T. Niu, L. Tao, B. Du, D. Li, Y. Wang, H. Dong, S. Zuo, B. Li, W. Shi, X. Ran, P. Li, H. Zhang, Z. Wu, C. Ran, L. Song, G. Xing, X. Gao, J. Zhang, Y. Xia, Y. Chen, W. Huang, Science 371 (2021) 1359–1364.
[41] J. Jeong, M. Kim, J. Seo, H. Lu, P. Ahlawat, A. Mishra, Y. Yang, M.A. Hope, F.T. Eickemeyer, M. Kim, Y.J. Yoon, I.W. Choi, B.P. Darwich, S.J. Choi, Y. Jo, J.H. Lee, B. Walker, S.M. Zakeeruddin, L. Emsley, U. Rothlisberger, A. Hagfeldt, D.S. Kim, M. Grätzel, J.Y. Kim, Nature 592 (2021) 381–385.
[42] X. Zhu, M. Du, J. Feng, H. Wang, Z. Xu, L. Wang, S. Zuo, C. Wang, Z. Wang, C. Zhang, X. Ren, S. Priya, D. Yang, S. Liu, Angew. Chemie - Int. Ed. 60 (2021) 4238–4244.
[43] T. Sen Su, F.T. Eickemeyer, M.A. Hope, F. Jahanbakhshi, M. Mladenović, J. Li, Z. Zhou, A. Mishra, J.H. Yum, D. Ren, A. Krishna, O. Ouellette, T.C. Wei, H. Zhou, H. H. Huang, M.D. Mensi, K. Sivula, S.M. Zakeeruddin, J.V. Milić, A. Hagfeldt, U. Rothlisberger, L. Emsley, H. Zhang, M. Grätzel, J. Am. Chem. Soc. 142 (2020) 19980–19991.
[44] D. Barrit, P. Cheng, K. Darabi, M.C. Tang, D.M. Smilgies, S. Liu, T.D. Anthopoulos, K. Zhao, A. Amassian, Adv. Funct. Mater. 30 (2020) 1907442.
[45] X. Wang, X. Ran, X. Liu, H. Gu, S. Zuo, W. Hui, H. Lu, B. Sun, X. Gao, J. Zhang, Y. Xia, Y. Chen, W. Huang, Angew. Chemie - Int. Ed. 59 (2020) 13354–13361.
[46] M. Li, C. Zhao, Z.K. Wang, C.C. Zhang, H.K.H. Lee, A. Pockett, J. Barbé, W.C. Tsoi, Y.G. Yang, M.J. Carnie, X.Y. Gao, W.X. Yang, J.R. Durrant, L.S. Liao, S.M. Jain, Adv. Energy Mater. 8 (2018) 1801509.
[47] Y. Wu, F. Xie, H. Chen, X. Yang, H. Su, M. Cai, Z. Zhou, T. Noda, L. Han, Adv. Mater. 29 (2017) 1–8.
[48] Y.H. Lin, N. Sakai, P. Da, J. Wu, H.C. Sansom, A.J. Ramadan, S. Mahesh, J. Liu, R.D. J. Oliver, J. Lim, L. Aspitarte, K. Sharma, P.K. Madhu, A.B. Morales-Vilches, P.K. Nayak, S. Bai, F. Gao, C.R.M. Grovenor, M.B. Johnston, J.G. Labram, J.R. Durrant, J.M. Ball, B. Wenger, B. Stannowski, H.J. Snaith, Science 369 (2020) 96–102.